

Effect of the Alumina Shell on the Melting Temperature Depression for Aluminum Nanoparticles

Valery I. Levitas,[†] Michelle L. Pantoya,^{*,‡} Garima Chauhan,[‡] and Iris Rivero[§]

Departments of Mechanical Engineering, Aerospace Engineering, and Material Science and Engineering, Iowa State University, Ames, Iowa 50011, Department of Mechanical Engineering, Texas Tech University, Lubbock, Texas 79409-1021, and Department of Industrial Engineering, Texas Tech University, Lubbock, Texas 79409-3061

Received: January 19, 2009; Revised Manuscript Received: June 22, 2009

The dependence of aluminum (Al) melting temperature on particle size was studied using a differential scanning calorimeter and thermogravimetric analyzer for particles encapsulated in an oxide shell. Pressure generation within the Al core leads to an increase in melting temperature in comparison with traditional melting temperature depression calculated using the Gibbs–Thomson equation. On the basis of elasticity theory, the pressure in the Al core at the onset of melting is caused mainly by surface tension at the alumina–air and Al–alumina interfaces. This implies that pressure due to the difference in thermal expansion of aluminum and alumina relaxes. A possible relaxation mechanism is discussed. The static strength of the alumina shell and the maximum static generated pressure in aluminum were evaluated. Mechanically damaging the oxide shell was shown to reduce the melting temperature due to a decrease in generated pressure within the Al core. Thus, reduction in melting temperature can be used as a quantitative measure of damage to the oxide shell. Results from X-ray diffraction studies show that 17-nm diameter Al particles had a 2-nm thick alumina shell in the γ -phase, while for a flat surface Al had an amorphous alumina shell stable to a thickness of 4 nm. Thus, pressure due to surface tension promotes denser γ -phases. Since particles with shells initially in the amorphous or γ -phase show the same flame speed and ignition delay time, fast oxidation observed under high heating rates cannot be explained by a phase transformation in the alumina shell. These findings have important implications for the melt-dispersion mechanism for fast Al oxidation.

1. Introduction

Size-dependent melting temperature depression has been demonstrated in many materials such as tin,^{1,2} gold,^{3–5} lead,^{6,7} indium,⁸ and aluminum.^{9–15} The dependence of melting temperature on particle size is not restricted to any particular material; rather, it encompasses a wide variety of materials from metals to semiconductors to molecular organic crystals.³ Eckert et al.⁹ showed with differential scanning calorimetry (DSC) that aluminum exhibits a size-dependent melting temperature depression reaching a minimum value of 836 K for 13-nm particles as compared to the bulk melting temperature of 933 K. The main reason for the size-dependent melting temperature depression is the increasing contribution of the surface energy to the energy balance at the nanoscale. The size-dependent melting temperature depression for small particles can be described using a thermodynamic approach which results in the Gibbs–Thomson equation^{16,17}

$$T_m^t = T_m(r) = T_m^b - \left\{ \frac{2T_m^b \sigma_{sl}}{\Delta H \rho_s r} \right\} \quad (1)$$

Here, $T_m(r)$ is the melting temperature for a particle of radius r (which we will call the theoretical melting temperature T_m^t),

T_m^b the bulk melting temperature, ΔH the bulk latent heat of fusion, ρ_s the solid phase density, σ_{sl} the solid–liquid interfacial energy. While there are more sophisticated models (reviewed for example in a previous study¹⁴), eq 1 is sufficient for our purposes.

Ideally, nanoparticles should behave in accordance with the theoretical behavior. But for nanoparticles embedded in a matrix of another material with a higher melting temperature, deviations from theoretical melting temperatures have been observed.^{8,13,14,18,19} The effect of an oxide shell on melting temperature is not well documented or understood. Decreases in melting temperatures measured by Sun and Simon¹⁴ (after correction for generated pressure) show good correspondence with the Gibbs–Thomson model (eq 1). Maximum depression was found to be about 13 K for Al particles with a diameter of 22 nm. In Trunov et al.,¹³ melting of particles of 44, 80, and 121 nm diameter (with 1.8–3.5 nm thick oxide shells) started 66 K below the bulk melting temperature, which (even allowing for the measured size distribution) cannot be interpreted in terms of any existing model. Both the above studies utilized DSC techniques. Mei et al.¹⁸ studied the superheating phenomenon in partially oxidized aluminum nanoparticles of 40–80 nm in diameter well encapsulated in thick alumina shells using X-ray diffraction (XRD) analysis. Their experimental results revealed that the encapsulated aluminum nanoparticles with different alumina shell thicknesses can be superheated to 7–15 K beyond the bulk equilibrium melting temperature of aluminum. They calculated the elevation in melting temperatures from the Clausius–Clapeyron equation and found it to be in agreement with experimentally observed superheating, demonstrating that superheating was

* To whom correspondence should be addressed. E-mail: michelle.pantoya@ttu.edu.

[†] Iowa State University.

[‡] Department of Mechanical Engineering, Texas Tech University.

[§] Department of Industrial Engineering, Texas Tech University.

induced by pressure build-up in the aluminum particle. Thus, one of the *goals* of this study is to experimentally analyze the influence of the oxide shell surrounding Al nanoparticles and the Al particle size dependence on the melting temperature to compare results with contradictory data in literature.

Pressure generated within the Al core due to the oxide shell's constraints is not well understood. Mei et al.¹⁸ investigated the effect of pressure in partially oxidized samples by growing the alumina shells to a considerable thickness (e.g., 18 nm). The change in distances between atomic planes were measured using XRD. Pressure was evaluated by multiplying bulk modulus by linear strain (change in distance between atomic planes divided by initial distance) and was in the range of 0.13–0.25 GPa. It may be possible that the actual pressure reported in ref 18 should be approximately three times higher because volumetric strain (the sum of linear strains in three orthogonal directions) rather than linear strain should be used to estimate pressure. Melting temperature and generated pressure were evaluated after completing the melting of the particles (i.e., when all X-ray peaks disappeared). In contrast, melting temperatures in DCS studies^{13,14} corresponded to initiation of the melting. In ref 18, the temperature at the start of the disappearance of X-ray peaks was 10–20 K below the bulk melting temperature, T_m^b . The pressure at the start of melting should be significantly lower than at the end because the volumetric melting strain is proportional to the concentration of molten Al in the particle.

Sun and Simon¹⁴ suggested a simplified equation for pressure build-up within the aluminum core; however, as further discussed below, they neglected the surface tensions at the Al–alumina and alumina–gas interfaces, which produce the main contributions for pressure generation. In this study, a more advanced equation derived in Levitas et al.^{20–22} for pressure estimation is used.

Pressure build-up within the Al core is an important element of the melt-dispersion mechanism for the reaction of Al nanoparticles.^{20–22} For fast heating (10^6 – 10^8 K/s) of Al nanoparticles, the oxide shell does not break before Al melts. Melting of the Al core is accompanied by a 6% volume increase that induces pressures on the order of 1–4 GPa. This magnitude of pressure build-up is made possible by the high dynamic strength alumina shell, which is only a few nm thick. Such high internal pressure results in the fracture and spallation of the alumina shell. After shell spallation, the pressure within the molten Al core is still 1–4 GPa, but at the surface it drops to approximately 10–20 MPa due to surface tension and gas pressure. The unbalanced pressure between the core and exposed surface creates an unloading wave that disperses the molten Al core into small clusters, the reaction of which with solid or gaseous oxidizer is not limited by diffusion through an oxide shell. Therefore, the interaction between the shell and core is critical to understanding and developing this mechanism. Along these lines, there are several issues related to this mechanism which will be addressed in this paper.

First, pressure build-up and its effect on melting point depend on the elastic properties and strength of the oxide shell. They in turn depend on whether the alumina shell is in an amorphous or crystalline γ -phase and whether the phase transformation from amorphous to γ phase occurs during heating. For slow heating rates the alumina shell goes through a series of phase transitions promoting a diffusive reaction mechanism. Trunov et al.²³ using thermogravimetric analysis (TGA) showed that the oxidation of aluminum nanoparticles at slow heating rates is a stepwise process. The amorphous alumina (Al_2O_3) shell transforms first

into γ - Al_2O_3 and then to α - Al_2O_3 crystalline polymorphs. These phase transformations are accompanied by a volume decrease and may cause fracture of the oxide shell. This point is used in ref 23 to explain the accelerated oxidation during the phase transformations. In addition, phase transformation has been assumed to play a key role in the diffusion model of Al oxidation at high heating rates.^{24,25} To shed light on the effect of phase transformations on the strength of the oxide shell and its relation to the oxidation mechanism, in this study the phase of the alumina shell in its initial state was determined using XRD and this information is used for data interpretation.

Second, damage of the oxide shell should reduce pressure build-up and its effect on melting temperature. This hypothesis was examined in this study by mechanically damaging the alumina shell and correlating this damage to melting temperature.

Third, one of the suggestions to improve performance of micrometer and nanoparticles was to increase the temperature of formation of the initial oxide shell in order to create initial compressive stresses in the shell and tensile stresses in the core.^{20–22} In this study we will analyze a possible relaxation of the internal stresses. During heating, high internal stresses are expected due to a difference in thermal expansion coefficients between Al and alumina. However, literature data are contradictory. As will be shown in section 3, internal stresses depend significantly on a relative particle diameter $M = r/\delta$ defined as the ratio of aluminum core radius (r) to the oxide shell thickness (δ). However, analysis of lattice spacing for samples with different M in Mei et al.¹⁸ does not show any appreciable difference for different M up to 860 K, which means that internal stresses relax. On the other hand, XRD study of the lattice strain²⁶ found the compressive strain between (111) planes of 0.017. Corresponding volumetric strain is a sum of three of the same strains between three mutually orthogonal (111) planes, i.e., it is very large at 0.051. Multiplying this strain by the Al bulk modulus at room temperature, $K = 75.2$ GPa, results in a large internal particle pressure of 3.84 GPa. In this study, we will estimate the magnitude of the internal stresses based on the increase in melting temperature with respect to the pressure-free case. Rai et al. (2004)²⁷ did a qualitative study on the importance of melting of aluminum in the oxidation of aluminum nanoparticles using hot-stage transmission electron microscopy (TEM) imaging to observe melting behavior. They found that aluminum melting causes rupture of the oxide shell and may be the primary initiator in the oxidation (and ignition) of aluminum nanoparticles. The stress relaxation problem will be addressed in this paper as well.

To summarize, two opposite effects are expected to be observed for melting of nanoparticles inside the strong shell: reduction in melting temperature with reduction in particle size according to the Gibbs–Thomson equation and increase in melting temperature due to pressure build-up in aluminum core before and during heating. Pressure may build up due to surface tension at the alumina–air and Al–alumina interfaces, due to lattice mismatch between Al and alumina (if alumina is in crystalline form) and due to difference in thermal expansion coefficients between Al and alumina. Some stress relaxation is expected based on known data.

It is also noted that the only existing routes that may minimize or control oxidation in aluminum particles involve controlling the atmosphere, such as using a vacuum or inert atmosphere.

2. Experimental Section

2.1. Materials. The powder aluminum samples ranged from 17 to 108 nm in average particle diameter, D , with physical

TABLE 1: Powder Manufacturer and Characteristics

particle diameter, D (nm)	manufacturer	alumina shell thickness, δ (nm)	M (r/δ)	active aluminum content, C (mass basis)	standard deviation (nm)
12000	Alfa Aesar	4.1	731.21	0.99	
202	Technanogy	3.4	28.70	0.84	
120	Technanogy	2.8	20.42	0.62	
108	Technanogy	3.9	12.84	0.73	56
80	NovaCentrix	2.0	18.60	0.80	
50	NovaCentrix	1.7	14.15	0.75	42
40	NovaCentrix	1.7	10.76	0.69	
25	Technanogy	1.8	6.03	0.54	21
17	Technanogy	1.9	3.47	0.38	12

characteristics and manufacturers listed in Table 1. All average particle diameters were calculated from BET (Brauner, Emmett, and Teller) surface area analysis (nitrogen gas adsorption method). In Table 1, the active aluminum content, C , is defined as the mass concentration of Al within Al + Al₂O₃ particles, which was provided by the manufacturers. The 108-nm Al alumina shell thickness was provided by Technanogy Inc. Alumina shell thicknesses and Al core radius for other particle sizes were calculated using the following equations

$$\delta = (R - r) \quad (2)$$

$$r = R \left[\frac{\rho_{\text{Al}_2\text{O}_3} C}{\rho_{\text{Al}} + C(\rho_{\text{Al}_2\text{O}_3} - \rho_{\text{Al}})} \right]^{1/3} \quad (3)$$

Here, $R=D/2$ is the radius of aluminum particle including shell, $\rho_{\text{Al}_2\text{O}_3}$ is the density of Al₂O₃ (3970 kg/m³), ρ_{Al} is the density of Al (2700 kg/m³), both at room temperature.

Statistical information regarding the particle size distribution was estimated from scanning electron microscopy (SEM) images using a secondary electron detector. The log-normal distribution's standard deviation from the average reported value is also listed in Table 1. The samples that were examined show an increasing trend in standard deviation with increasing average particle size. Samples without a standard deviation were not available for this statistical analysis. Figure 1a shows a representative image for 108 nm aluminum particles size distribution. All samples consist of spherically shaped particles. Most of the particles lie close to the average particle size provided by the manufacturer. A representative SEM image was also taken for damaged 108 nm particles

(Figure 1b), which show that damaging the oxide shell did not alter the shape of the particles, the average particle size, or agglomeration.

To create imperfections in the alumina shell the particles were damaged mechanically. A thin layer of aluminum powder was placed between two cylindrical steel pistons 7 cm in diameter. The pistons were placed on the press bed of the ENERPAC hydraulic press, and a vertical load of 4.5 kN was applied to the powder with the single acting cylinder of the press. The top cylindrical piston was rotated by 45° about the axial direction repeatedly to create imperfections in the alumina shell.

2.2. DSC. The melting behavior of aluminum nanoparticles was studied using a NETZSCH STA 409 PC Luxx differential scanning calorimeter integrated with a thermogravimetric analyzer. The uncertainty in measurements for the DSC is ± 0.2 °C and for the TGA is $\pm 0.3\%$. This uncertainty is based on the temperature calibration, instrument sensitivity, and repeatability of the following experiments, as discussed below. These systematic errors are on the same order of magnitude as the instruments resolution.

Temperature calibration was performed using ASTM metal standards of aluminum, gold, indium, tin, and zinc. Sensitivity calibration was carried out using a standard 0.25 mm thick sapphire sample for which the specific heat and mass were known. In addition, a baseline correction was generated by running a specific heating program with an empty sample and reference crucible. The correction curve value was subtracted from the true sample DSC curve to obtain a heat flow curve without the effect of buoyancy.

Melting temperatures were measured for each aluminum sample using a constant heating rate of 10 K/min. Five milligrams of each sample was measured with a digital scale up to an accuracy of ± 0.1 mg and placed in a platinum sample crucible with an alumina liner, such that the entire base of the crucible was evenly covered with the sample ensuring good thermal contact. The sample and reference crucibles were covered with a platinum lid containing a pinhole. The pinhole allows for gas escape upon phase change or reaction produced from the sample.

The DSC was evacuated up to a pressure of less than 1.9×10^{-4} mbar and backfilled with argon at a purge gas flow rate of 42.5 mL/min and a balance protection gas flow rate of 25.5 mL/min. The sample was heated using a temperature program which consisted of a dynamic heating segment from 293 to 1073 K. The sample was heated at a heating rate of 10 K/min.

Melting temperature is defined as the extrapolated onset temperature which is the point where the auxiliary line through the descending peak slope intersects the baseline. This definition for melting temperature is used because the value is less dependent on heating rate and sample properties, such as thermal conductivity, mass, and sample thickness.²⁸ The STA 409 PC

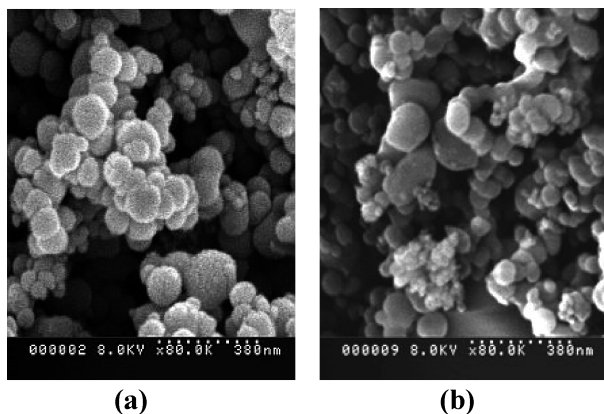


Figure 1. SEM image for (a) undamaged and (b) damaged 108 nm aluminum powder.

TABLE 2: Pressure Build Up in Aluminum Nanoparticles

R (nm)	T_m^t (K)	T_m^u (K)	ΔT_m^u (K)	T_m^d (K)	ΔT_m^d (K)	p (GPa)	ΔP^u (GPa)	ΔP^d (GPa)
50.1	928.7	933.2	4.6	931.6	2.9	0.063	0.078	0.049
38.1	927.1	929.1	2.1	927.2	0.2	0.091	0.033	0.003
23.3	922.9	926.1	3.2	919.6	-2.3	0.136	0.055	
18.3	919.9	924.6	4.7	922.6	2.7	0.166	0.081	0.046
10.7	910.1	927.9	17.8	925.8	15.7	0.239	0.303	0.267
6.6	895.5	919.2	23.7	912.5	17	0.312	0.403	0.289

Proteus software was used to measure the extrapolated onset temperature from the heat flow graph.

2.3. Validation of Mechanical Damage in Alumina Shell.

Limitations in the resolution of the SEM facilities did not enable observation of fractures, imperfections, and damage to the alumina shell (see Figure 1b). Also, damaged places may heal quickly when exposed to air by reacting with oxygen. It is assumed that such a healing process will not completely recover the strength of the oxide shell and that some defects still remain. As an alternative approach to validate shell damage after mechanical loading, a further series of heat flow curves were produced. In this series of experiments the aluminum particles were heated in an oxygen environment. A comparison was then made between the amount of exothermic energy associated with the Al–oxygen reaction for undamaged and damaged particles. Damage of the alumina shell may expose small portions of the aluminum core to surrounding oxidizer or create channels for easier diffusion such that diffusion and reaction will occur at room temperature immediately after damage. In this process the shell “heals”, thickens, and the active aluminum content decreases. In this way, the amount of aluminum available for the aluminum–oxygen reaction is reduced such that the corresponding heat of reaction will also be reduced. By comparing the heats of reaction for undamaged and damaged particles, the degree of shell damage can be inferred by the reduced magnitude of the heat of reaction associated with less aluminum content. Also, the percentage of mass gain in the TGA curve will be indicative of the mass increase due to formation of alumina which in turn indicates the percent of aluminum reacted. Five milligram samples from each particle size were heated in the STA 409 PC in an oxygen environment with a heating rate of 10 K/min from 293 to 1643 K with a gas flow rate of 68 mL/min (25.5 mL/min for balance protection gas and 42.5 mL/min for purge gas). Heat flow and mass loss curves for damaged and undamaged powders were measured and compared.

2.4. XRD Characterization. XRD patterns were collected at room temperature with a Proto LXR system on Al_2O_3 as-received samples featuring five distinct particulate sizes: 17, 80, 120, 202, and 12 μm . An X-ray tube with a Copper anode (Cu K α radiation wavelength, $\lambda = 1.5418$) was operated at 30 kV and 7 mA while collecting measurements. The planes selected for diffraction were (311), (400), and (440) corresponding to the strongest diffraction planes of the cubic crystalline structure of $\gamma\text{-Al}_2\text{O}_3$. XRD detectors were set to scan between three established ranges of 2θ angles corresponding to (1) 24–40°, (2) 41–56°, and (3) 64–80° to collect diffracted X-rays from the (311), (400), and (440). Sixty exposures were collected per location for 0.5 s of duration per exposure with maximum β angle of 30° and nine β angle tilts.

3. Results and Discussion

3.1. Size Dependence of Melting Temperature and the Pressure Effect. Table 2 summarizes the temperature and pressure results. R represents the particle radius, T_m^t the theoretical melting temperature for a particle of radius r (eq 1), T_m^u and ΔT_m^d represent the melting temperatures for undamaged and damaged particles, respectively, ΔT_m^u and ΔT_m^d represent the difference between theoretical and experimental melting temperatures for undamaged and damaged particles, respectively, pressure p is determined using elasticity theory (eq 7), and ΔP_u and ΔP_d are the pressures calculated using the Clausius–Clapeyron equation (eq 6) for undamaged and damaged particles, respectively.

The melting temperatures for aluminum nanoparticles were observed to reduce as the particle size decreases (Table 2 and Figure 2). There was around a 14.5 K reduction in the melting temperature (919.2 K) of the sample of smallest particle size as compared to bulk melting temperature of aluminum (933.67 K). Our results are consistent with those of Sun and Simon¹⁴ and differ significantly from Trunov et al.¹³

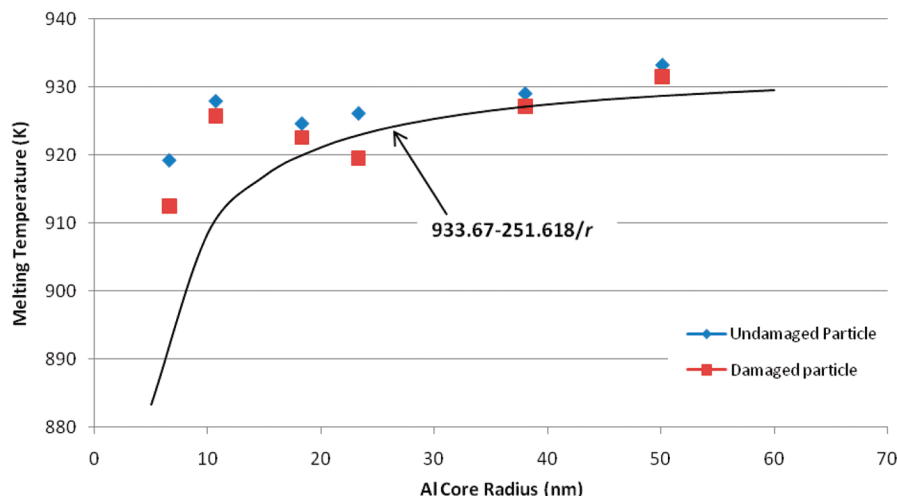


Figure 2. Aluminum melting temperature vs aluminum core radius r . Experimental data for undamaged and damaged particles and theoretical curve $T_m^t = 933.67 - 251.618/r$ calculated using the Gibbs–Thomson equation (eq 2).

A comparison of experimental melting temperatures with Gibbs–Thomson model (Table 2 and Figure 2) reveals that the measured values are higher than theoretical values, as expected due to the effect of pressure. The Gibbs–Thomson curve was generated using eq 1 with $T_m^b = 933.67$ K, $\rho_s = 2530$ kg/m³ (at melting temperature, see Table 3),²¹ $\Delta H = 396$ J/g,²⁹ $\sigma_{sl} = 0.135$ J/m². Values of σ_{sl} vary in literature in the range 0.093–0.163 J/m²,^{11,19} so an intermediate value close to that range^{11,19} was used. Damaging the alumina shell reduced the measured value of melting temperatures.

The elevated melting temperatures for particles inside the alumina shell can be explained with the Clausius–Clapeyron equation, which describes the relationship between pressure build-up and the elevation in melting temperatures

$$\Delta P = \Delta T \frac{\Delta H}{T_m^b} \left[\frac{\rho_s \rho_l}{\rho_s - \rho_l} \right] \quad (4)$$

Here, ΔP is the pressure build up with respect to atmospheric pressure, ΔT the difference between melting temperatures of particles and the theoretical melting temperatures, $\rho_l = 2380$ kg/m³ the liquid phase density of aluminum at melting. Upon substituting the referenced values, eqs 5 and 6 can be expressed in simplified terms

$$T_m^t = 933.67 - \frac{251.618}{r} \quad (5)$$

$$\Delta P = 0.017 \Delta T \quad (6)$$

where r is in nm, ΔP is in GPa, and ΔT is in K. Values of ΔT and ΔP for undamaged and damaged particles are given in Table 2. Because of a pressure build-up within the aluminum core, an increase in melting temperature is observed for aluminum nanoparticles in comparison with the values determined in eq 5. When the alumina shell is damaged by grinding, the effect of pressure build-up decreases. As a result the melting temperatures also reduce and approximate the theoretical values. The values for pressure obtained from the Clausius–Clapeyron equation were compared to the pressure values calculated using the equation for pressure in an aluminum sphere, p , derived in refs 20 and 21 based on elasticity theory.

$$p = \frac{12(m^3 - 1)(\epsilon_2^i - \epsilon_1^i)G_2K_1K_2}{H} + \frac{2K_1(4G_2 + 3m^3K_2)\Gamma_1}{rH} + \frac{(2\Gamma_2 + p_g r)m^2K_1(4G_2 + 3K_2)}{rH} \quad (7)$$

Here the subscript 1 denotes alumina and 2 aluminum; Γ_1 is the surface tension at the aluminum–alumina interface, and Γ_2 is the surface tension between alumina and air; p_g is the external gas pressure which will be neglected in calculations; $m = 1 + \delta/r = 1 + 1/M$; G and K are the shear and bulk moduli respectively, $K_1 = fK_1^m + (1 - f)K_1^s$ is the bulk modulus of the molten Al/solid Al mixture; f is the volume fraction of molten

Al; subscripts s and m are for solid and molten phases, and $H = 3m^3K_1K_2 + 4G_2(K_1 + (m^3 - 1)K_2)$. Inelastic strains can be given by^{20,21}

$$\epsilon_1^i = -(\alpha_1^s(T_m - T_0) + (1 - f)\alpha_1^s(T - T_m) + f\alpha_1^m(T - T_m) + f\epsilon^m); \epsilon_2^i = -\alpha_2(T - T_0) \quad (8)$$

Here α is the linear thermal expansion coefficient, T the current temperature, T_0 the temperature at which the alumina shell was formed, T_m the bulk melting temperature, and ϵ^m the linear (i.e., $1/3$ of volumetric) expansion during the melting of Al. Lattice mismatch between Al and alumina lattices (for crystalline alumina only) can be easily taken into account in eq 8. However, we do not have data to specify it, and it relaxes similar to thermal strains (see below).

Pressure increase within the core of aluminum particles can be described by a combination of the following factors: surface energy at the interface of air–alumina, surface energy at the interface of alumina–aluminum, volumetric expansion during melting, and differences in thermal expansion coefficients of aluminum and alumina. The effect of the surface energy at the interface of solid–liquid aluminum on the melting temperature is neglected in comparison with the effect of Γ_1 and Γ_2 , because it is 1 order of magnitude smaller. Since we consider initiation of melting, we can put $f = 0$. The main parameter that determines pressure in the Al core is the temperature, T_0 , at which the alumina shell was formed. If T_0 is equal to room temperature, the pressure will be much higher than calculated based on eq 4 and experimental values of ΔT . Sun and Simon¹⁴ fit their experimental values assuming $T_0 = 888$ K, i.e., 45 K below the melting temperature. They interpreted such high T_0 because of pressure relaxation during the phase transformation from amorphous to crystalline, so T_0 should be taken as the end temperature of this transformation. Stress relaxation during phase transformation is generally a plausible assumption, but there are distinct points which must be addressed, especially for nanoparticles. First, Sun and Simon¹⁴ did not take into account surface tension at the aluminum–alumina interface and between alumina and air, which as we will see below is a significant contribution and further increases T_0 toward the melting temperature. Second, for an oxide shell thicker than 4–5 nm, the shell is initially in crystalline form (see also experimental data in section 3.4), i.e., the stress relaxation cannot be connected to crystallization. To find the lower bound for generated pressure, we say $T = T_m = T_0$ and obtain

$$p = \frac{2K_1}{rH}(\Gamma_1(4G_2 + 3m^3K_2) + \Gamma_2m^2(4G_2 + 3K_2)) \quad (9)$$

Table 3 contains the material parameters collected in ref 21 used for calculating pressure values for all particle sizes. It was assumed $\Gamma_1 = \Gamma_2 = \Gamma = 1.05$ GPa nm = 1.05 J/m², similar to previous reports.^{20–22} In Table 3, G and K are the shear and bulk moduli, respectively, α is the linear thermal expansion coefficient, ϵ^m is the linear (i.e., $1/3$ of volumetric) expansion during the melting of Al, ρ is the mass density; superscripts s

TABLE 3: Material Parameters at Melting Temperature $T = T_m$ ²¹

K_1^s (GPa)	K_1^m (GPa)	K_2 (GPa)	G_2 (GPa)	α_1^s (10^5 K ⁻¹)	α_1^m (10^5 K ⁻¹)	α_2 (10^5 K ⁻¹)	ϵ^m	Γ (GPa nm)	ρ_l^s (kg/m ³)	ρ_l^m (kg/m ³)
71.1	41.3	234.8	149.5	3.032	4.268	0.778	0.02	1.05	2530	2380

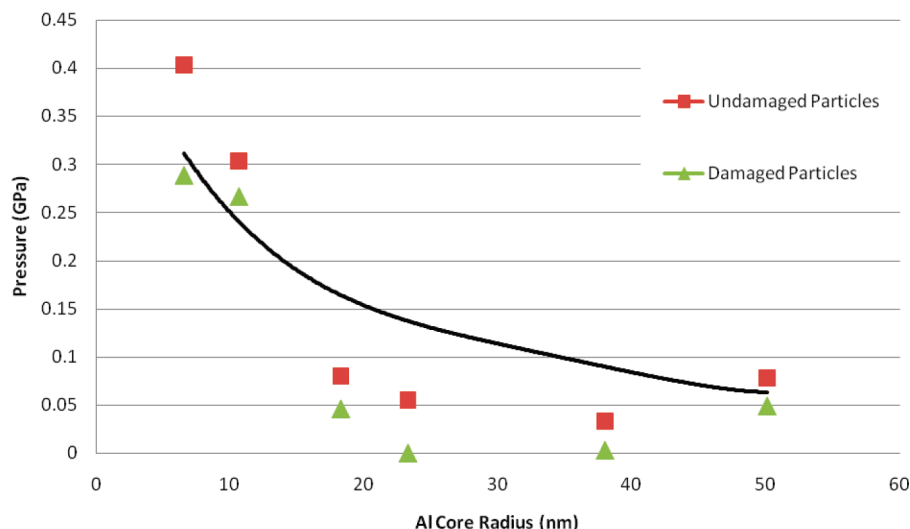


Figure 3. Comparison between pressures build-up within aluminum core vs aluminum core radius r . Line corresponds to the calculated pressure using elasticity theory (eq 9). Points are calculated using the Clausius–Clapeyron equation (eq 6) for undamaged ΔP^u and damaged ΔP^d particles based on melting temperatures from Table 2.

and m are for solid and molten phases; subscripts 1 and 2 are for aluminum core and alumina shell.

To the authors' knowledge surface energy data for amorphous alumina is not reported in the literature. Interface energies for sapphire reported in the literature³⁰ have significant scatter and the above values are in the range of reported data. Table 2 contains calculated values of pressure p . Figure 3 shows three pressures as a function of aluminum particle radius, namely, the pressure calculated using elasticity theory and the pressure calculated using the Clausius–Clapeyron equation for measured melting temperatures of undamaged and damaged particles.

Figure 3 shows that the pressure caused by surface tension at the aluminum–alumina interface and between alumina and air give a reasonable estimate for pressure determined by the Clausius–Clapeyron equation. When pressure based on the Clausius–Clapeyron equation for undamaged particles, ΔP^u , is above the pressure, p , due to surface tension (particles with $D = 17, 24.9$, and 108 nm), the pressure due to thermal expansion did not relax completely. For particles with $D = 24.9$ nm, the pressure due to thermal expansion did not relax completely even after damage. Note that, for comparison, the thermal pressure due to differences in thermal expansion coefficients for $T_0 = 300$ varies from 1.57 GPa for $M = 3.47$ to 0.58 GPa for $M = 18.6$, i.e. much higher than the difference between ΔP^u and p . For all other particles, the pressure p due to surface tension exceeds pressure based on the Clausius–Clapeyron equation, i.e., it also partially relaxes. This result opens the issue of identifying the stress relaxation mechanism due to slow heating. The first possibility is related to diffusion of aluminum atoms into the alumina shell. The second is related to stress relaxation due to damage of the oxide shell. The third is that stress relaxation is caused by phase transformation in the alumina shell. However, as we will see in section 3.3, the second and third possibilities cannot be completely responsible for stress relaxation, which add credit to the first hypothetical mechanism. The question of whether internal stresses relax at high heating rates of 10^8 K/s typical for flame propagation rates on the order of 1 km/s, remains open.

3.2. Oxidation Heat and Mass for Undamaged and Damaged Nanoparticles. A greater reduction in pressure indicates a higher degree of shell damage and vice versa. To validate shell damage, undamaged and damaged particles were heated

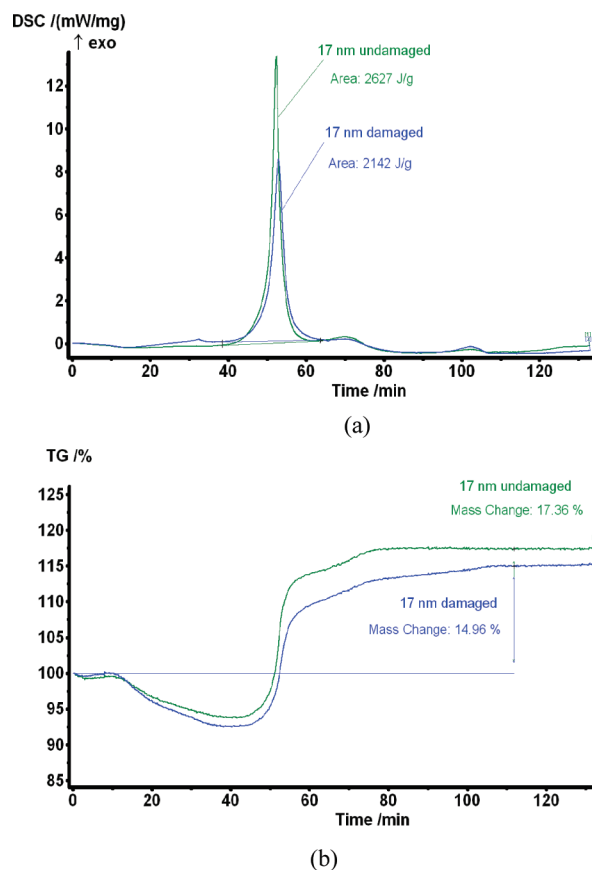


Figure 4. (a) Heat flow and (b) thermogravimetric curves for undamaged and damaged 17 nm Al particles.

in the DSC in an oxygen environment. Figure 4a shows energy liberated during oxidation for damaged and undamaged 17 nm particles evaluated as the area under the heat flow oxidation curve. The area under the curve for damaged particles is less than that for undamaged particles, which indicates that less aluminum is present in the damaged particles to react with oxygen compared to undamaged particles. Reduced aluminum content in the damaged particles indicates healing of the damaged oxide shell, validating shell damage.

Shell damage was also validated by comparing TGA graphs for undamaged and damaged particles. Figure 4b shows graphs

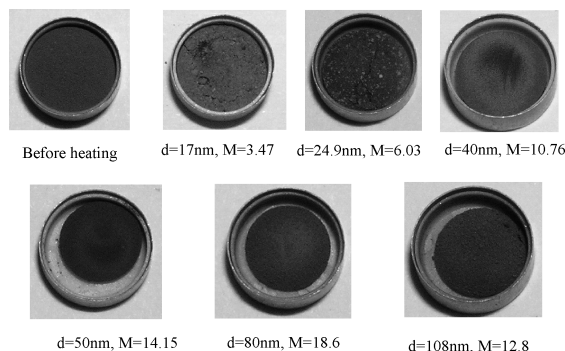


Figure 5. Shrinkage in powders due to sintering was more pronounced for larger particles compared to smaller particles.

for mass change with respect to temperature. Undamaged particles gain $(2.4/17.26) 100 = 13.86\%$ more mass than damaged particles, which means more aluminum was present in the undamaged particles to react with oxygen. Less aluminum content in damaged particles shows the effect of “healing”, that caused some aluminum to react with air.

3.3. Oxide Fracture after Complete Melting. Figure 5 shows the shrinkage of aluminum particles of different sizes after complete melting in the DSC. The shrinkage is negligible for 17 nm particles, small for 24.9 and 40 nm particles, and very pronounced for 50, 80, and 108 nm particles. The most probable interpretation is that the alumina shell ruptures, molten aluminum flows outward, and fills the voids between the particles. Capillary forces pull particles toward each other and lead to an overall reduction in volume of the powder, effectively sintering particles together. The fracture of the oxide shell and flow of liquid aluminum out of the shell was observed in the a TEM study previously reported.²⁷ Previous results^{20–22} show that, as particle radius and $M = r/\delta$ increase, hoop stresses in the shell increase and that there is a larger probability of fracture of the oxide shell, which is consistent with the observations in Figure 5.

Because of particle size distributions for each average diameter shells for larger particles in each distribution were broken while the shells of smaller particles were not broken. Since there is no visible difference between 17 nm Al particles before heating and after melting (Figure 5), their oxide shells did not break after melting. Almost the same shrinkage for particles of 50, 80, and 108 nm in diameter implies that most shells were broken. Then shells for most of the 24.9 and 40 nm particles were not ruptured after melting. Thus, thermal stress relaxation during heating below the melting temperature, discussed in section 3.1, cannot be explained by damage of the oxide shell, because even volume increase due to melting does not damage the shell in small particles. Since the shell of 17 nm particles does not undergo an amorphous to γ -phase transformation, phase transformation cannot be the universal reason for stress relaxation.

In consideration of those particles with a diameter of 17–40 nm which did not break, we can estimate the ultimate strength σ_u of the shell and pressure in Al liquid using equations for hoop stress (equal to σ_u) and pressure in a liquid droplet from.²¹ For completely relaxed thermal stresses (i.e., $T_0 = T_m$) and nonrelaxed stresses due to complete melting (which correspond to different changes in interatomic distances for different M in¹⁸), the estimates for the static strength and generated pressure are presented in Table 4. The oxide shell possesses static strength in the range of 2.06–4.90 GPa and can withstand pressures in the range 1.14–1.83 GPa. Such levels of pressure, if released

TABLE 4: Estimated Ultimate Strength of the Oxide Shell and Pressure Generated inside the Liquid after Melting

D (nm)	σ_u (GPa)	p (GPa)
17	2.06	1.83
25	3.58	1.52
40	4.90	1.14

quickly, are sufficient to initiate the melt-dispersion mechanism.^{20,21} Note that our estimates for the dynamic strength at high heating (and consequently loading) rates is 11.3 GPa,^{21,22} which is comparable to estimated theoretical strength σ_{th} .

3.4. XRD Analysis of As-Received Particles. Analysis of the five Al_2O_3 samples XRD patterns derived from the 24–40° scan (refer to Figure 6) reveal that peaks of crystalline γ - Al_2O_3 were found for all samples with the exception of those exhibiting particulate sizes corresponding to 80 nm and 10–14 μm . It is important to note that diffraction from very small crystals, such as those analyzed in this research, result in broadening of the diffracted beam;³¹ that is, diffraction occurs at angles that are near but not identical to the Bragg angle. Figure 7 depicts the XRD pattern of a γ - Al_2O_3 sample with a particulate size of 17 nm. From this figure the crystalline peak of γ - Al_2O_3 is clearly defined at 45.9° corresponding to the strong diffraction of the (400) plane. Figure 8 depicts the XRD patterns derived from the 72° Bragg angle where no peaks of crystalline γ - Al_2O_3 are observed for samples exhibiting particulate sizes of 17 and 80 nm. Therefore, upon a complete assessment of the XRD patterns shown in Figures 6, 8, it can be deduced that samples with a particulate size of 80 nm and 10–14 μm (which were the only samples where no crystalline peaks were observed in the XRD

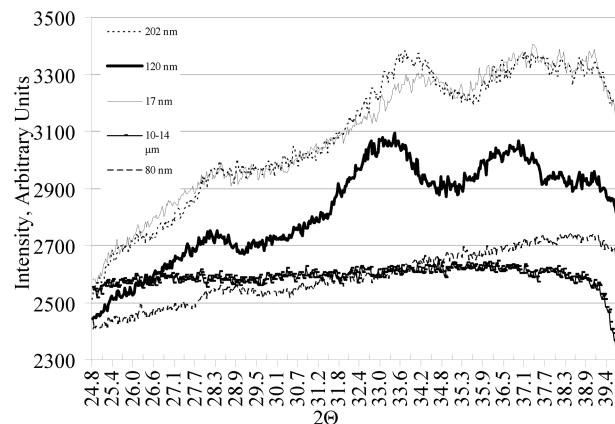


Figure 6. XRD patterns from diffraction between 24 and 40° Bragg angles of Al_2O_3 exhibiting various particulate sizes.

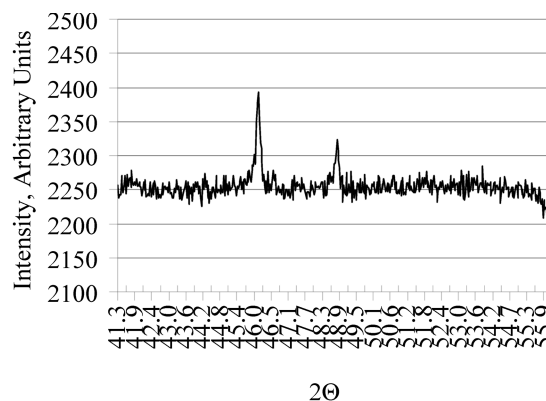


Figure 7. XRD pattern from diffraction between 41 and 56° Bragg angles of Al_2O_3 exhibiting a particulate size of 17 nm.

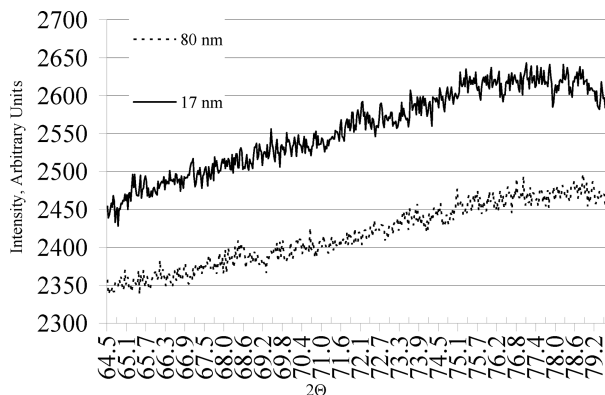


Figure 8. XRD patterns from diffraction between 64 and 80° Bragg angles of Al_2O_3 exhibiting particulate sizes of 17 and 80 nm.

patterns) exhibit an amorphous structure. In addition, with the exception of samples exhibiting a particulate size of 17 nm in Figure 7, diffracted peaks exhibit a broad maximum that is indicative of nanocrystalline materials with relatively large concentration of (amorphous) grain boundaries and nonhydrostatic lattice strain.

These results have several consequences.

(1) It is well accepted that for flat surfaces of alumina at room temperature the amorphous oxide shell is stable below 4 nm, and above 4 nm the crystalline phase is stable. Our results show that for alumina curvature as large as for 17 nm particles transition to crystalline phase occurs for shell thickness of 2 nm. Because transformation of amorphous phase into $\gamma\text{-Al}_2\text{O}_3$ is accompanied by 17% of volume reduction, pressure $4\Gamma_2/D = 0.25$ GPa caused by the surface tension between alumina and air promotes this phase transformation.

(2) In Figure 9, flame velocity and relative flame velocity (i.e., flame velocity divided by a maximum flame velocity for the given set up) are presented as a function of particle size and M , based on results in ref 22. All experimental points are close to the theoretical curve based on the melt-dispersion mechanism. In particular, for $M < 19$, the flame velocity reaches a maximum value and is independent of M . Results presented in Figures 6–8 show that for Al particles of 120 nm in diameter and an oxide shell of 4 nm (i.e., $M = 14$), the shell was in the γ phase initially. For smaller particle sizes and oxide shells, the shell was initially amorphous. Also, ignition times for nano-Al particles with an oxide shell smaller than 3.4 nm (which are

in the amorphous phase) and from 4.5 to 7.7 nm (which are in the γ phase) are approximately the same for $M < 19$.^{20,21} Thus, nanoparticles demonstrate the same maximum possible reactivity in terms of flame velocity, ignition delay time, and consequently, reaction time, independent of whether the oxide shell is in an amorphous or γ phase (i.e., whether phase transformation from amorphous to γ phase occurs or not). These results indicate that phase transformation is not the reason for short reaction times, which is in contradiction with the phase-transformation-based models.^{24,25} In these models,^{24,25} short ignition times result from oxide shell fracture caused by the presence of the phase transformation. Results presented here are consistent with experimental kinetics data for amorphous- γ phase transformation,³² according to which complete phase transformation time at a temperature of 1573 K is 6 orders of magnitude larger than the transformation time calculated.^{24,25}

(3) Predictions based on the melt-dispersion mechanism are quite sensitive to the mechanical properties of the shell, especially to the shell strength. Thus, the same flame velocity for amorphous and crystalline shells implies that shell strength for both are close under the loading rate typical for these experiments (i.e., 10^8 K/s).

4. Conclusion

Our experimental results on the dependence of melting temperature on the size of aluminum nanoparticles encapsulated in an oxide shell are consistent with experiments in ref 14 and differ from results in ref 13. The melting temperature is higher than predicted by the Gibbs–Thomson equation, which is rationalized by pressure generation and its effect on the melting temperature according to the Clausius–Clapeyron equation. By use of elasticity equations, the pressure in the aluminum at the start of melting is caused mainly by surface tension at the alumina–air and aluminum–alumina interfaces. This means that thermal stresses below melting relax, in correspondence with experimental data in ref 18. The mechanism of stress relaxation is not clear. We speculate that it is diffusion of aluminum atoms from core into shell, partially driven by internal pressure. Damage of the oxide shell, including damage caused by phase transformation in the shell, cannot be completely responsible for the pressure relaxation, because for 17 nm particles pressure relaxation does not occur even after complete melting and for some particle sizes, the shell was initially in a crystalline phase. Preliminary mechanical damaging of the oxide shell reduces

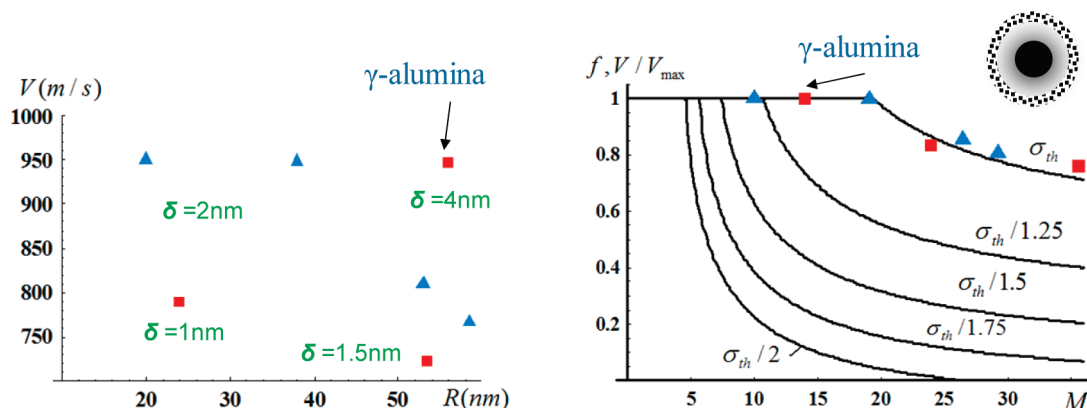


Figure 9. Flame speed vs Al particle core radius (left) and flame speed divided by $V_{\max} = 950$ m/s vs relative Al core radius $M = R/\delta$ (right) for several oxide shell thicknesses. For various oxide shell strengths (shown near the curves in terms of fraction of theoretical strength $\sigma_{th} = 11.3$ GPa) the lines correspond to the volume fraction of melt, f , necessary to fracture of the oxide shell.^{20–22} Good correspondence between relative flame speed and f is observed. Marked experimental points are obtained for shell in the γ -phase; other points are for the amorphous shell. Adopted with modifications from ref 22.

the melting temperature due to a decrease in the generated pressure within the particle core. Damage and partial healing were confirmed by oxidation heat and mass measurements. Thus, reduction in melting temperature can be used as a quantitative measure of damage to the oxide shell for study of its effect on the melt-dispersion mechanism. We also discussed the mechanism of fast reaction of aluminum nanoparticles during fast heating based on fracture of the oxide shell induced by amorphous to γ -phase transition in the oxide shell.^{24,25} Since particles with shells initially in amorphous and γ -phases show the same flame speed and ignition delay time, the reaction mechanism cannot be explained by the shell's phase transformation. If the melt-dispersion mechanism is operative, independence of the particle's reactivity on the oxide shell phase means that that amorphous and γ -phases have comparable mechanical properties, specifically dynamic ultimate strength. Also, XRD studies indicated that for 17 nm particles the alumina shell with thickness of 2 nm is in γ -phase, while for a flat surface the amorphous alumina is stable up to a 4 nm thickness.

We found that the oxide shell for a particle with relatively small M does not break even at complete melting of aluminum. This allowed estimates of static strength of alumina in the range of 2.06–4.90 GPa and that the shell can withstand pressures in the range 1.14–1.83 GPa. Such a level of pressure, if released quickly, is sufficient to initiate the melt-dispersion mechanism.^{20–22}

Acknowledgment. M. Pantoya and G. Chauhan gratefully acknowledge support and encouragement by Dr. Ralph Anthenien and the Army Research Office Contract No. W911NF-04-1-0217. The authors also gratefully acknowledge support from the National Science Foundation under Contract No. CBET-0755236, managed by Dr. Phillip Westmoreland and the Office of Naval Research under Contract Nos. N00014-07-1-0318, N00014-08-1-1262, and N00014-08-1-0104, all managed by Dr. Clifford Bedford.

References and Notes

- (1) Wronski, C. R. M. *Brit. J. Phys.* **1967**, *18*, 1731–1737.
- (2) Bachels, T.; Guntherodt, H. J.; Schafer, R. *Phys. Rev. Lett.* **2000**, *85*, 1250–1253.
- (3) Dick, K.; Dhanasekaran, T.; Zang, Z.; Meisel, D. *J. Am. Chem. Soc.* **2001**, *124*, 2312–2317.
- (4) Buffat, P. H.; Borel, J.-P. *Phys. Rev. A* **1976**, *13* (6), 2287–2298.
- (5) Castro, T.; Reifengerger, R.; Choi, E.; Andres, R. P. *Phys. Rev. B* **1990**, *42* (13), 8548–8556.
- (6) Peters, K. F.; Chung, Y.-W.; Cohen, J. B. *Appl. Phys. Lett.* **1997**, *71* (16), 2391–2393.
- (7) Peters, K. F.; Cohen, J. B.; Chung, Y.-W. *Phys. Rev. B* **1998**, *57* (21), 13430–13438.
- (8) Dippel, M.; Maier, A.; Gimble, V.; Wider, H.; Evenson, W. E.; Rasera, R. L.; Schatz, G. *Phys. Rev. Lett.* **2001**, *87* (9), 0955051–0955054.
- (9) Eckert, J.; Holzer, J. C.; Ahn, C. C.; Fu, Z.; Johnson, W. L. *Nanostruct. Mater.* **1993**, *2*, 407–413.
- (10) Jang, J. S. C.; Koch, C. C. *J. Mater. Res.* **1990**, *5* (2), 325–333.
- (11) Allen, S. L.; Lai, J. R. A.; Carlsson, L. H. *Appl. Phys. Lett.* **1998**, *72*, 1098.
- (12) Patterson, B. M.; Unruh, K. M.; Shah, S. I. *Nanostruct. Mater.* **1992**, *1* (1), 65.
- (13) Trunov, M. A.; Umbrajkar, S. M.; Schoenitz, M.; Mang, J. T.; Dreizin, E. L. *J. Phys. Chem.* **2006**, *110*, 13094–13099.
- (14) Sun, J.; Simon, S. L. *Thermochim. Acta* **2007**, *463*, 32–40.
- (15) Puri, P.; Yang, V. *J. Phys. Chem. C* **2007**, *111*, 11776–11783.
- (16) Skripov, V. P. *Phys. Stat. Solidi (a)* **1981**, *66*, 109.
- (17) Hanszen, K.-J. *Z. Phys.* **1960**, *157*, 523.
- (18) Mei, Q. S.; Wang, S. C.; Cong, H. T.; Jin, Z. H.; Lu, K. *Acta Mater.* **2005**, *53*, 1059–1066.
- (19) Chattopadhyay, K.; Goswami, R. *Prog. Mater. Sci.* **1997**, *42*, 287–300.
- (20) Levitas, V. I.; Asay, B. W.; Son, S. F.; Pantoya, M. L. *Appl. Phys. Lett.* **2006**, *89*, 071909–1–071909–3.
- (21) Levitas, V. I.; Asay, B. W.; Son, S. F.; Pantoya, M. L. *J. Appl. Phys.* **2007**, *101* (8), 083524.
- (22) Levitas, V. I.; Pantoya, M. L.; Dikici, B. *Appl. Phys. Lett.* **2008**, *92*, 011921.
- (23) Trunov, M. A.; Schoenitz, M.; Zhu, X.; Dreizin, E. L. *Combust. Flame* **2004**, *140*, 310–318.
- (24) Trunov, M. A.; Schoenitz, M.; Dreizin, E. L. *Combust. Theory Model.* **2006**, *10* (4), 603–623.
- (25) Trunov, M. A.; Umbrajkar, S. M.; Schoenitz, M.; Mang, J. T.; Dreizin, E. L. *J. Phys. Chem. B* **2006**, *110*, 13094–13099.
- (26) Ramaswamy, A. L.; Kaste, P. *J. Energ. Mater.* **2005**, *23*, 1.
- (27) Rai, A.; Lee, D.; Park, K.; Zachariah, M. R. *J. Phys. Chem. B* **2004**, *108*, 14793–14795.
- (28) Hohne, G.; Hemminger, W.; Flammersheim, H.-J. *Differential Scanning Calorimetry. An Introduction for Practitioners*; Springer-Verlag: Berlin, Heidelberg, New York.
- (29) Incropera, F. P.; DeWitt, D. P. *Fundamentals of heat and mass transfer*; John Wiley & Sons: New York, 1996.
- (30) Levi, G.; Kaplan, W. D. *Acta Mater.* **2003**, *51*, 2793–2802.
- (31) Cullity, B. D.; Stock, S. R. *Elements of X-Ray Diffraction*, 3rd ed.; Prentice Hall: Upper Saddle River, NJ, 2001.
- (32) Merzhanov, A. G.; Grigorjev, Y. M.; Gal'chenko, Y. A. *Combust. Flame* **1977**, *29* (1), 114.

JP902317M